frontiers | Frontiers in Physiology

TYPE Original Research
PUBLISHED 03 January 2024
DOI 10.3389/fphys.2023.1271254

OPEN ACCESS

EDITED BY
Alex Bhogal,
Utrecht University, Netherlands

REVIEWED BY
Luis Hernandez-Garcia,
University of Michigan, United States
Michael Germuska,
Cardiff University, United Kingdom

*CORRESPONDENCE
Sriranga Kashyap,
sriranga.kashyap@uhn.ca
Kâmil Uludağ,
kamil.uludag@uhn.ca

RECEIVED 02 August 2023
ACCEPTED 27 November 2023
PUBLISHED 03 January 2024

CITATION
Kashyap S, Oliveira ÍAF and Uludağ K (2024), Feasibility of high-resolution perfusion imaging using arterial spin labeling MRI at 3 Tesla.
Front. Physiol. 14:1271254.
doi: 10.3389/fphys.2023.1271254

Feasibility of high-resolution perfusion imaging using arterial spin labeling MRI at 3 Tesla

Sriranga Kashyap[1]*, Ícaro Agenor Ferreira Oliveira[1] and Kâmil Uludağ[1,2,3,4,5]*

[1]Krembil Brain Institute, University Health Network, Toronto, ON, Canada, [2]Department of Medical Biophysics, University of Toronto, Toronto, ON, Canada, [3]Center for Neuroscience Imaging Research, Institute for Basic Science, Suwon, Republic of Korea, [4]Department of Biomedical Engineering, Sungkyunkwan University, Suwon, Republic of Korea, [5]Physical Sciences, Sunnybrook Research Institute, Toronto, ON, Canada

Cerebral blood flow (CBF) is a critical physiological parameter of brain health, and it can be non-invasively measured with arterial spin labeling (ASL) MRI. In this study, we evaluated and optimized whole-brain, high-resolution ASL as an alternative to the low-resolution ASL employed in the routine assessment of CBF in both healthy participants and patients. Two high-resolution protocols (i.e., pCASL and FAIR-Q2TIPS (PASL) with 2 mm isotropic voxels) were compared to a default clinical pCASL protocol ($3.4 \times 3.4 \times 4\ mm^3$), all of whom had an acquisition time of ≈ 5 min. We assessed the impact of high-resolution acquisition on reducing partial voluming and improving sensitivity to the perfusion signal, and evaluated the effectiveness of z-deblurring on the ASL data. We compared the quality of whole-brain ASL acquired using three available head coils with differing number of receive channels (i.e., 20, 32, and 64ch). We found that using higher coil counts (32 and 64ch coils as compared to 20ch) offers improved signal-to-noise ratio (SNR) and acceleration capabilities that are beneficial for ASL imaging at 3 Tesla (3 T). The inherent reduction in partial voluming effects with higher resolution acquisitions improves the resolving power of perfusion without impacting the sensitivity. In conclusion, our results suggest that high-resolution ASL (2 to 2.5 mm isotropic voxels) has the potential to become a new standard for perfusion imaging at 3 T and increase its adoption into clinical research and cognitive neuroscience applications.

KEYWORDS

arterial spin labeling, brain perfusion, high spatial resolution, 3 Tesla, RF coil, neuroimaging frontiers

1 Introduction

Arterial spin labeling (ASL) is a non-invasive neuroimaging technique that uses magnetically labeled arterial blood water as an endogenous tracer to measure cerebral blood flow (CBF) (Detre et al., 1992; Williams et al., 1992). ASL provides a safe and repeatable method for assessing brain state and function without any risk of toxicity or allergic reactions from exogenous contrast agents. ASL can also be utilized to assess the quantitative CBF in units of mL/100 g/min at an individual voxel level (Williams et al., 1992; Buxton et al., 1998).

In recent years, technological advances in MRI scanner hardware and software, and new cutting-edge analysis methods have positively impacted the range of ASL applications and

resulted in a notable increase in the number of publications (Detre et al., 2012; Iutaka et al., 2023; Lindner et al., 2023). Another factor for its increasing popularity in clinical research is the community effort to standardize acquisition methods, data structures, and analyses (Alsop et al., 2015; Clement et al., 2022; Hernandez-Garcia et al., 2022). However, widely adopted standards (e.g., described in the ASL "white paper" (Alsop et al., 2015)) prescribe spatial resolutions of 3–4 mm in-plane and 4–8 mm slice thickness for ASL scans that are maximally 5–6 min long (typical length of clinical research/standard-of-care MRI protocols) but may not be optimal anymore with current hardware and MRI sequences. Although these protocols may suffice for macroscopic effects (such as pattern of large regions of hypo-perfusion), they are insufficient to detect subtle abnormalities that may represent early stage of neurological diseases or small lesions (Mora Álvarez et al., 2019). Therefore, ASL at higher spatial resolution (< 3 mm nominal, isotropic) is highly desirable.

Another reason for going to high spatial resolutions is to reduce partial volume (PV) effects, which occur when the voxel signal contains fractional contributions from more than one tissue type, for example, gray matter (GM), white matter (WM), and cerebrospinal fluid (CSF). This can introduce inaccuracies in perfusion quantification of the tissue of interest, resulting in either or both underestimation and over-estimation, depending on the PV fractions in the voxels. For instance, Asllani et al. (2008) showed that a voxel mixture of 80:20% gray:white matter (this ratio would be inclusive after the threshold, in most cases) would result in a 24% perfusion underestimation. Another example is the study by Donahue et al. (2006), investigating the impact of a higher resolution ASL protocol compared to low-resolution positron emission tomography (PET) scans, and they demonstrated that uncorrected CBF PET images might underestimate the gray matter (GM) CBF by 20%. In fact, in 2006, Donahue et al. actually envisioned the future of ASL imaging at 3 Tesla (3 T) to be spatial resolutions of 2.5 mm in-plane or higher. Seventeen years later, 3 T ASL imaging is still routinely carried out with voxel sizes > 3 mm, and the voxels are almost never isotropic, which can lead to underestimation of lesions and even misdiagnosis in the direction of the lowest spatial resolution. Although there have been methods and algorithms developed that can provide a means to *post hoc* correct for PV effects (Kirk et al., 2020a; Kirk et al., 2020b; Chappell et al., 2021), they usually cannot recreate lost information, and therefore, the most straight-forward and preferred approach is to just acquire the data at higher spatial resolutions.

This is notwithstanding high-resolution ASL studies carried out at field strengths higher (4.7 T, 7 T) than those typically used in the clinic (1.5 T, 3 T). For example, Mora Álvarez et al. (2019) demonstrated the feasibility of a high-resolution continuous ASL (CASL) at 4.7 T within a clinical time frame of 6 min. The study also observed reduced PV averaging at $1.5 \times 1.5 \times 3$ mm^3 resolution. Another interesting example is the study published by Zuo et al. (2013) where they employed Turbo-FLASH (fast low angle shot) ASL, both pseudo-continuous ASL (pCASL) and pulsed ASL (PASL) at 7 T showing the feasibility of achieving an in-plane resolution of 0.85×1.7 mm^2. At 7 T, recent functional MRI (fMRI) studies also showed the feasibility of using perfusion-weighted contrast with ASL at sub-millimeter spatial resolutions of 0.9 mm isotropic (Kashyap et al., 2021) and 0.7 mm isotropic (Ivanov et al., 2018; Kashyap et al., 2022) using a 3D-EPI (Poser et al., 2010) readout with a FAIR (Kim, 1995) QUIPSS II (Wong et al., 1997; Wong et al., 1998) labeling scheme.

Although there is evidence of the transformative potential that ultra-high-field scanners can have for clinical research and cognitive neuroscience applications, they are limited in availability compared to the ubiquity of 3 T scanners. Therefore, a translation of high-resolution ASL to widely available 3 T clinical platforms is urgently needed to catalyze clinical research as well as further advance the standards of care. This requires systematic optimization attuned to easily accessible workflows, which is currently not explored in the existing ASL literature.

The current study addresses these aforementioned challenges and gaps in the literature by first developing, testing, and evaluating high-resolution ASL protocols at 3 T in clinically feasible times, and then it compares them to a vendor default protocol that is typically used in routine clinical scanning. To this end, we developed optimized 2 mm isotropic pCASL and PASL protocols that balance the trade-off between signal-to-noise ratio (SNR) and acquisition time (TA) to be feasible for clinical application (TA ≈ 5 min). Furthermore, we also evaluated the impact of the choice of standard head coils on 3 T perfusion imaging. We systematically evaluated our protocols and the clinical default protocol with all three commercially available head coils (20-channel head and neck coil, 32-channel head coil only, and 64-channel head and neck coil) to ascertain the optimal hardware for high-resolution acquisitions. In addition, we quantify and demonstrate the reduction in partial voluming enabled by the high-resolution acquisitions. Finally, the lengthening of the readout with 3D-GRASE is recognized to result in through-plane (z-axis) blurring, resulting in loss of spatial resolution (Tan et al., 2011; Paschoal et al., 2021). We also assess the impact of advanced post-processing methods such as z-deblurring to improve spatial fidelity of the acquired data.

2 Materials and methods

2.1 Participants

Eight healthy volunteers (four female and four male volunteers, mean age = 29 ± 4 years) participated in the study and provided written informed consent prior to scanning. All participants were screened healthy individuals, non-smokers, not taking any medications, and with no history of neurological or neurovascular conditions. All procedures in this study conformed to the standards set by the Declaration of Helsinki and was approved by the Research Ethics Board of University Health Network according to the guidelines of Health Canada.

2.2 Data acquisition

Data were acquired on a Siemens MAGNETOM Prisma 3 T MRI scanner (Siemens Healthineers, Erlangen, Germany) at the Slaight

Family Centre for Advanced MRI (Toronto Western Hospital, Toronto ON, Canada); the scanner has a maximum gradient strength of 80 mT/m and a slew rate of 200 T/m/s, and runs on the XA30A IDEA software platform. We used three commercial MRI coils, namely, a 20ch head and neck coil, a 32ch head coil only, and a 64ch head and neck coil for receiving, and the transmission was carried out by the body coil. Participants were positioned by taking the eye centers as a reference for the magnet isocentering to minimize B_0 offsets for the labeling in the neck. All data of participants were acquired in the same scan session. The participants were brought out of the scanner, coils were exchanged, and the participants were repositioned to the magnet's isocenter. The sequential order of coils was pseudo-randomized between participants to avoid any systematic biases.

2.2.1 Anatomical imaging

Structural scans were acquired with the 32ch head coil. Whole-brain anatomical data were acquired using a 3D multi-echo magnetization-prepared rapid gradient echo (3D-MEMPRAGE) sequence (van der Kouwe et al., 2008) that uses volumetric EPI navigators combined with selective data reacquisition (Tisdall et al., 2012) to produce (prospectively) motion-corrected T_1w images (Tisdall et al., 2016) that were used in the study. The 3D-MEMPRAGE data were acquired at 0.8 mm isotropic resolution (TI = 1000 ms, TEs_{1-4} = 1.81, 3.6, 5.39, 7.18 ms, TR = 2500 ms, α = 8°, 208 sagittal slices, matrix = 320 × 320, GRAPPA = 2, Ref. lines = 32, partial $Fourier_{slice}$ = 6/8, echo spacing = 11.2 ms, bandwidth = 740 Hz/px, turbo factor = 168, total acquisition time ≈ 8 min). The four echoes were combined (using root mean squares, RMS) into a high-fidelity T_1-weighted image following the scanner's on-line reconstruction. Quantitative T_1 mapping was carried out using a 3D magnetization-prepared 2 rapid gradient echoes (3D-MP2RAGE) sequence (Marques et al. 2010). The MP2RAGE T_1 maps were only used to facilitate perfusion quantification and thus were acquired at a 1.2 mm isotropic resolution (TIs_{1-2} = 700, 2500 ms, α_{1-2} = 4°, 5°, TE = 4.04 ms, TR = 3200 ms, 144 axial slices, matrix = 192 × 192, GRAPPA = 2, Ref. lines = 32, partial $Fourier_{phase}$ = 6/8, echo spacing = 9.08 ms, bandwidth = 150 Hz/px, turbo factor = 144, total acquisition time ≈ 4 min). T_1 maps were calculated in-line using the Siemens MapIt package (Siemens Healthineers, Erlangen, Germany).

2.2.2 Perfusion imaging

All ASL protocols were developed using the Siemens Advanced 3D-ASL work-in-progress (WIP) sequence (courtesy of Siemens Healthineers, Erlangen, Germany) available for the XA30A baseline platform. The ASL data were acquired with a segmented 3D-GRASE readout for improved SNR (Fernández-Seara et al., 2008; Feinberg et al., 2009; Vidorreta et al., 2014). Three ASL protocols were acquired per coil in each participant: 1) the clinical default protocol (3.4 × 3.4 × 4 mm^3, "Clinical" in Table 1), 2) a high-resolution (or hires) pCASL protocol (2 mm isotropic, 'Hires' in Table 1), and 3) a hires PASL protocol employing a FAIR-Q2TIPS (Luh et al., 1999) labeling scheme (2 mm isotropic, "PASL Hires" in Table 1). For clinical and hires ASL variants, two steady-state magnetization (M_0) calibration images were acquired without any labeling, but with matched readout and TR increased to 20 s, one of M_0 had the opposite phase encoding for distortion correction. The new hires protocols developed in this study were acquired in approximately the same total time as the spatially anisotropic clinical ASL scan (≈ 5 min).

2.3 Data processing

2.3.1 Anatomical imaging

The RMS-combined, motion-corrected, T_1-weighted 3D-MEMPRAGE was processed using FreeSurfer v 7.3.2 (Dale et al., 1999; Fischl et al., 1999; Fischl et al., 2002) (https://surfer.nmr.mgh.harvard.edu/) using a brain mask that was generated using *mri_synthstrip* (Hoopes et al., 2022) and was provided as an additional input to the *recon-all* pipeline.

2.3.2 Perfusion imaging

The first volume of the ASL timeseries was discarded as separate M_0 scans had been acquired for quantification. The pre-processing steps were carried out using FSL (Smith et al., 2004) included motion and distortion correction, where all control and label volumes were independently realigned to the first volume of the ASL scan. The separately acquired M_0 scans were rigidly registered to the first volume of the ASL scan, and then distortion correction was performed using FSL's *topup* (Andersson et al., 2003) with the two M_0 images. The perfusion timeseries was calculated using sinc-subtraction as implemented in FSL's *perfusion_subtract*. The M_0 images, perfusion-weighted data, and the MP2RAGE T_1 maps (co-registered to M_0) were used as input to *oxasl* (Chappell et al., 2009) (https://github.com/physimals/oxasl) for voxelwise perfusion quantification. M_0 images were co-registered to the anatomical image using FreeSurfer's *bbregister* (Greve and Fischl, 2009) to obtain CBF maps in both native and structural space. No adaptive spatial smoothing (Groves et al., 2009) or partial volume correction (Chappell et al., 2011) was applied. Next, all anatomical scans were carefully registered to the 1 mm isotropic MNI non-linear 2009c asymmetric template space (Fonov et al., 2009; 2011) using the ANTs SyN algorithm (Avants et al., 2014; 2011) (https://github.com/ANTsX/ANTs). Native space maps from *oxasl* were resampled in a single step to the MNI space using *antsApplyTransforms*. The stability of the perfusion signal over time (temporal SNR, tSNR) was calculated dividing the temporal mean by the temporal standard deviation of the perfusion-weighted data (also referred to as perfusion tSNR). The SNR (consequently, tSNR) of a voxel is expected to scale proportionally with its volume, and this condition makes it challenging to compare datasets of highly different spatial resolutions. Therefore, to better appreciate the tSNR relative to a dataset's spatial resolution, the perfusion tSNR map from the hires scan was scaled by the ratio of the voxel volumes of clinical to hires datasets (46.24 mm^3/8 mm^3 = 5.78).

2.3.3 Partial volume analysis

In order to visualize the impact of the higher spatial resolution acquisition, participant-wise T_1-weighted images were resampled to the nominal spatial resolution of the clinical protocol (3.4 × 3.4 × 4.0 mm^3) or the hires protocol (2.0 mm isotropic). The resampled T_1-weighted images were segmented using FSL's *fsl_anat*

TABLE 1 Sequence parameters for the three ASL protocols in the present study.

Parameter	Clinical	Hires	PASL hires
Labeling	pCASL	pCASL	FAIR-Q2TIPS
TR/TE_{eff}	4720/20.40 ms	4000/16.80 ms	4000/16.80 ms
Tag control pairs	12	12	12
BS	Gray–White strong	Gray–White	Gray–White
Bolus (TI_1)/PLD (TI_2)	1800/1800 ms	1600/1800 ms	700/1800 ms
FOV	220 × 220	192 × 192	192 × 192
Matrix	64 × 64	96 × 96	96 × 96
Slice oversampling	20%	22.5%	22.5%
Acceleration	GRAPPA 2	2D-CAIPI 3	2D-CAIPI 3
Slices	30	66	66
Partial Fourier	Off	6/8 yz	6/8 yz
Bandwidth	2442 Hz/px	1930 Hz/px	1930 Hz/px
Echo spacing[1]	0.49 ms	0.68 ms	0.68 ms
EPI factor	31	23	23
Segments (k_z)	3	3	3
Turbo factor[2]	12	20	20
Echo-train length[3]	245 ms	336 ms	336 ms
Acquisition time	05:09 min	05:11 min	05:11 min

Although the study focuses on the two pCASL protocols, the PASL protocol is included here for completeness.
TR, repetition time; TE, echo time; FA, flip angle; BS, background suppression (gray–white = 2, gray–white strong = 4 non-selective pulses); PLD, post-labeling delay; TI, inversion time (for PASL); FOV, field-of-view.
[1] echo spacing, time between echoes in the 2D readout;
[2] turbo factor, number of echoes acquired after excitation;
[3] echo-train length≈TE×turbo factor.

(Zhang et al., 2001) to obtain PV estimates. The cortical gray matter segmentation from FreeSurfer was morphologically dilated by one voxel and resampled to the two resolutions, and this resampled, dilated cortical mask was used as the ROI for the PV analyses. To this end, we used a histogram-based analysis to first sort the voxels into different PV fraction bins. Then, to compare the two different acquisition resolutions, the number of voxels in each histogram bin was scaled by their voxel volumes of 46.24 mm^3 and 8 mm^3, respectively, for the clinical and hires protocols, giving us the volume of PV voxels in each bin. This normalization enabled a direct comparison of the PV. A difference between the hires and clinical histograms (after rescaling) was computed for all values above a PV fraction threshold of 0.5 for each of the three tissue classes, namely, GM, WM, and CSF.

2.3.4 Deblurring analysis

In an additional analysis, ASL data acquired from the 32ch coil were pre-processed using *oxasl_deblur* (https://github.com/physimals/oxasl_deblur). We evaluated two different methods for deblurring the data, namely, fast Fourier transform division (FFT) and Lucy–Richardson deconvolution (Lucy) as implemented in *oxasl_deblur*, with three different kernel options (direct estimation, Lorentzian, and Lorentzian with a Weiner filter). Smoothness of the deblurred data was estimated using AFNI's (Cox, 1996; Cox and Hyde, 1997) *3dFWHMx* (Cox et al., 2017) function.

3 Results

3.1 Comparison of clinical and hires ASL data

Figure 1 shows the group average absolute CBF (in units of mL/100 g/min) maps from clinical and hires pCASL protocols presented in three orthogonal views (middle panel) for the three

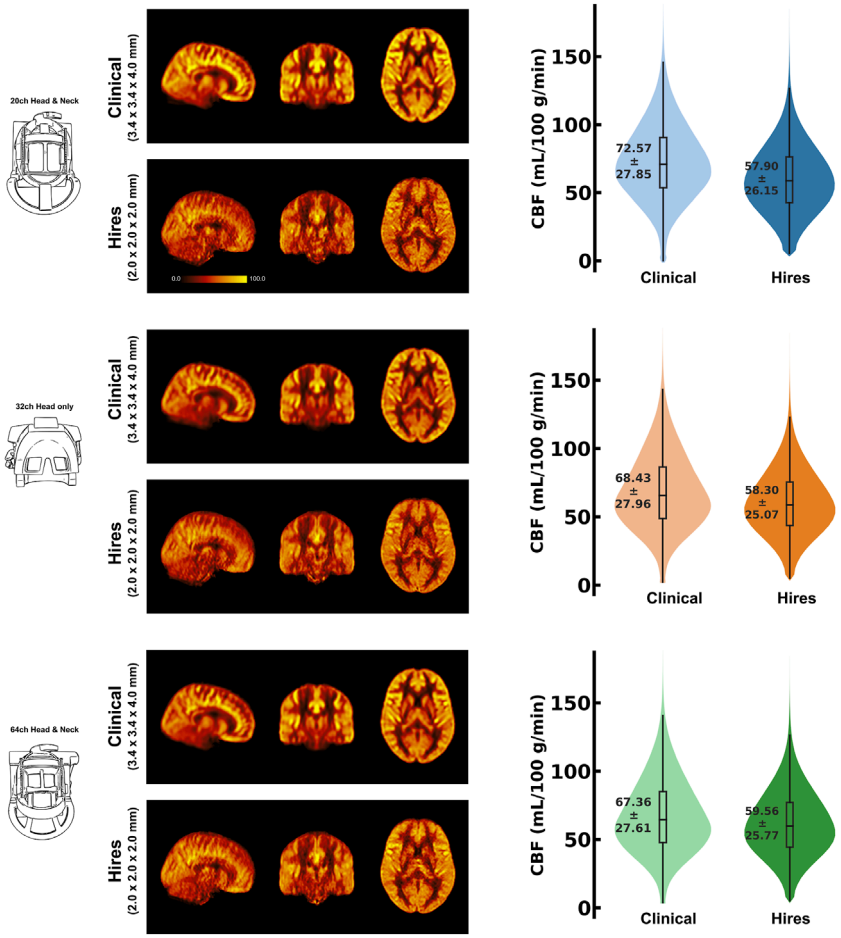

FIGURE 1
Mosaic of orthogonal views of the group average (n = 8) CBF (in mL/100 g/min) for data acquired using the three respective head coils (drawing on the left). In the middle column, the maps obtained from the clinical and hires pCASL acquisitions are displayed in the top and bottom rows, respectively. (Right) Violin plots of the CBF distribution across all participants' data (n = 8) for the two acquisitions. The annotation represents the mean ± standard deviation of the distribution.

head coils used to acquire the data (drawing in left panel). The panel on the right shows the distribution of the CBF values in GM across the participants' data as a violin plot with the CBF values represented on the *y*-axis for the two protocols. The figure annotation represents the mean ± standard deviation of the distribution. A comparison of the group average perfusion weighting and relative CBF (rCBF, in arbitrary units) for the two protocols and three head coils is shown in Supplementary Figure S1. It is important to note that the rCBF calculated using *oxasl* is the perfusion-weighted image (PWI) following kinetic model inversion (i.e., one step before M_0 calibration to physiological units of mL/100 g/min) and is not relative to the whole brain mean or normal white matter (Chappell et al., 2023). For the clinical and hires protocols, we observe that the mean CBF values are very similar for all three coils. The CBF values obtained from the clinical protocols are ≈ 17% greater than those obtained from the hires data, and both measures are in the acceptable range for healthy volunteers (Alsop et al. 2015). Summary statistics for all the different perfusion metrics calculated from the data are tabulated in Supplementary Tables S2–S6.

3.2 Analysis of the partial voluming

One of the primary advantages of acquiring higher spatial resolution data is the reduction of the partial voluming of the signal of interest. As shown in Figure 2, the differences in voxel volumes (hires−clinical) are plotted at each partial volume fraction bin ranging from 0.5 to 1.0 (50% to "pure" single-tissue composition) for three tissue classes, that is, GM (a), WM (b), and CSF (c), using a dilated GM ROI. Data from each participant are shown as a colored dot, with the mean across participants plotted as a black dashed line. In Figure 2A, we observe that on average, above a PV fraction of 0.6 (60% GM), there is a net positive change in the volume of GM and remains positive for all higher PV fractions. In other words, even within the dilated GM ROI, there is a larger volume (total ≈ 6713 mm^3) of "pure" GM in hires than in the clinical data; therefore, partial voluming is reduced. This finding is corroborated by the spatial maps of PV, as illustrated in the right panels with the PV map of hires and clinical shown on top and bottom rows, respectively. A similar pattern is observed in Figures 2B, C that

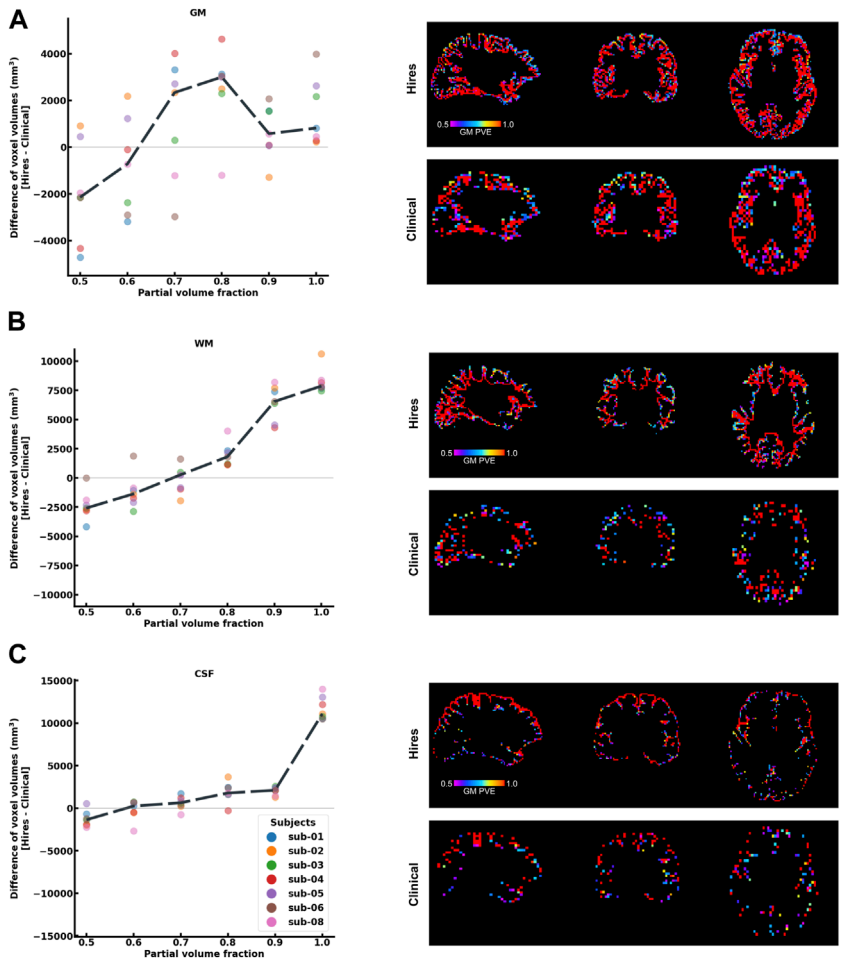

FIGURE 2
Histogram difference plot for all bins ≥0.5 threshold of PV fraction for **(A)** GM, **(B)** WM, and **(C)** CSF tissue classes of the hires and clinical acquisitions. Value from each participant is represented as a color-coded circle, and the group average is plotted as a black dotted line. A single-participant PV estimate map is shown in the right panel for the clinical and hires spatial scales, spatially illustrating the findings of the histogram analysis. It is to be noted that sub-07 is excluded from this analysis as *fsl_anat* could not be completed.

quantifies the PV in WM and CSF, respectively. In other words, within the dilated GM ROI used to extract these results, there is a significantly larger volume of "pure" WM (total ≈ 16,938 mm^3) and "pure" CSF (total ≈ 15,422 mm^3). As GM is bound on either side with WM and CSF, we can infer that the greater the number of "pure" non-GM voxels, the lower the amount of voxels which are PV with GM, and this finding is corroborated by the spatial maps of PV.

3.3 Deblurring analysis of 3D-GRASE ASL

Table 2 shows that the effective spatial resolution of both the clinical and hires datasets is different from what is indicated in the protocol, also referred to as the nominal spatial resolution (in this study, $3.4 \times 3.4 \times 4.0\ mm^3$ and 2.0 mm isotropic, respectively). Systematic evaluation of five parameter combinations in *oxasl_deblur* (Supplementary Table S2) shows that all five combinations result in an improvement in a reduction in the full width at half maximum (FWHM). We found that using the FFT method with direct kernel estimation yields the smallest effective FWHM (clinical: 6.38 ± 0.33 mm vs. hires: 2.38 ± 0.13 mm, Supplementary Table S2). Table 2 shows FWHM estimated from AFNI's *3dFWHMx* for x, y, and *z* axes as well as the effective FWHM (ACF). We observe that irrespective of the acquisition resolution, the smoothness is maximal along the *z*-axis (clinical: 8.73 ± 0.65 mm, hires: 4.01 ± 0.31 mm), and this is the axis along which *oxasl_deblur* is most effective, reducing the smoothness estimate to 5.22 ± 0.49 mm and 1.41 ± 0.12 mm for clinical and hires data, respectively. The change in the estimated FWHM along z after deblurring ($\Delta FWHM_{clinical}/\Delta FWHM_{hires}$) is 1.35 times larger for the hires dataset than that for the clinical data. Figure 3 shows the group average CBF maps for the clinical and hires datasets before ("orig") and after ("deblurred") deblurring, and the distribution of CBF values across all participants' data is also shown as a violin plot.

TABLE 2 FWHM (in mm) estimated using AFNI's *3dFWHMx* for the clinical and hires 3D-GRASE datasets deblurred using the FFT method and direct kernel estimation as implemented in *oxasl_deblur*.

FWHM	Clinical	Clinical deblurred	Hires	Hires deblurred
x	5.51 ± 0.27	5.49 ± 0.76	3.08 ± 0.18	2.65 ± 0.21
y	6.24 ± 0.20	5.91 ± 0.55	2.85 ± 0.17	2.42 ± 0.22
z	8.73 ± 0.65	5.22 ± 0.49	4.01 ± 0.31	1.41 ± 0.12
ACF	10.08 ± 0.67	7.24 ± 0.58	4.83 ± 0.36	2.69 ± 0.12

A comparison of FWHM for different deblurring methods can be found in Supplementary Table S2.
Numerical values presented are mean ± std. dev across participants.

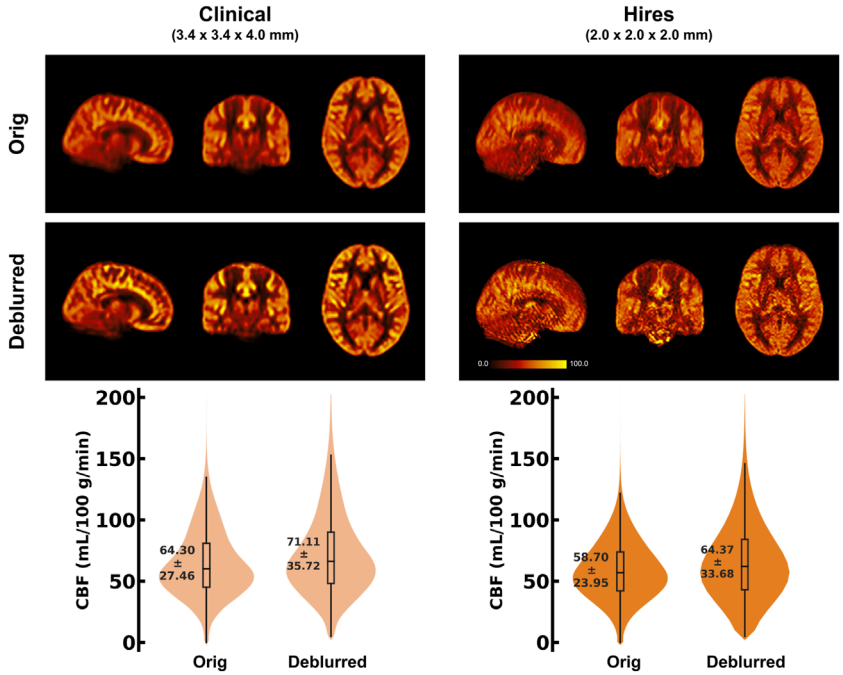

FIGURE 3
(Top) Orthogonal views of the group average CBF maps (in mL/100 g/min) (n = 8) obtained using the 32-channel head coil, before and after deblurring using the FFT method and direct kernel estimation as implemented in *oxasl_deblur*. (Bottom) Violin plots of the CBF distribution across all participants' data (n = 8) for the two acquisitions before and after deblurring. The annotation represents the mean ± standard deviation of the distribution.

3.4 Impact of head coil choice for imaging perfusion

Figure 1 demonstrates that robust CBF maps can be acquired independently of the coil choice. However, the spatial distribution of the CBF maps from the hires protocol shows a preference for 32 and 64ch. Figure 4 (top and middle rows) illustrates the impact of perfusion tSNR across the three coils. In the case of the clinical protocol, the increasing coil count has ≈ 2–2.5% gain in perfusion tSNR, whereas the hires protocol has ≈ 34–42% gain in perfusion tSNR with increasing coil count (Supplementary Table S5). The perfusion tSNR maps of the hires data, rescaled by the ratio of voxel volume (Figure 4, bottom row), illustrate the improvement of tSNR with 32 and 64 coils over 20ch. In addition, Supplementary Table S4 shows that the inter-quartile range (IQR) of the perfusion weighting increases with increasing coil count (20/32/64 ch: for clinical, 312.50/334.30/338.79 a. u., and for hires, 386.34/423.67/440.03 a. u.) for both protocols. The IQR of perfusion weighting between the three coils behaves similarly with the hires PASL protocol (20/32/64 ch: 396.12/447.66/454.97 a. u., Supplementary Table S9). Therefore, it is the SNR benefits afforded by higher coil count rather than the quality or type of labeling used that is responsible of the improvement in the higher IQR of perfusion values.

4 Discussion

In this study, we demonstrate that it is feasible to measure perfusion robustly and repeatably using ASL at a high spatial resolution of 2 mm isotropic within clinically feasible times of

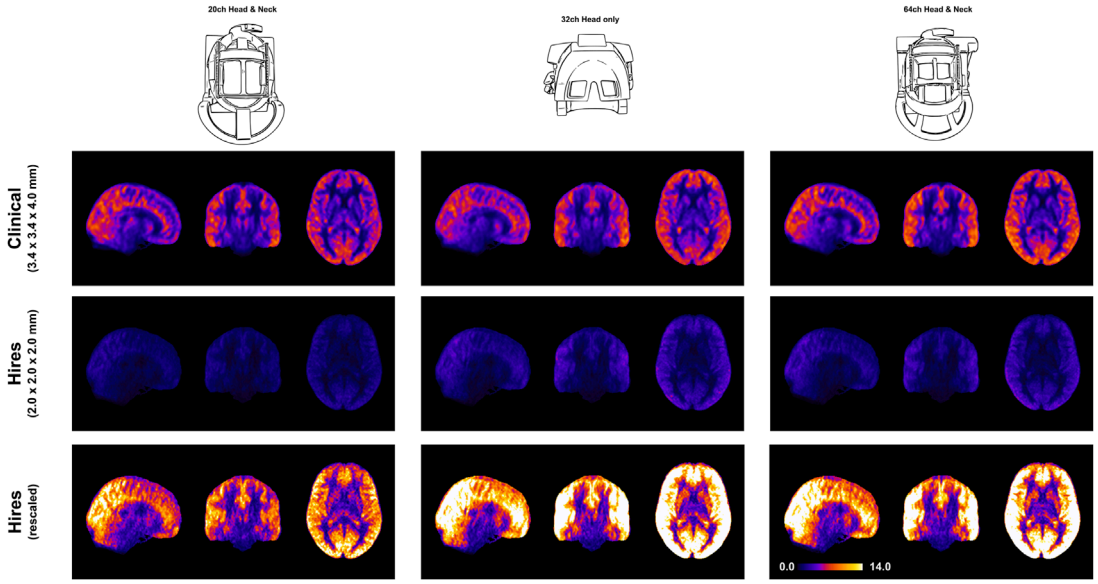

FIGURE 4
Orthogonal views of the group average perfusion tSNR maps (n = 8) where the pCASL clinical and hires maps are presented in the top and middle rows, respectively. The bottom row shows the hires tSNR data (middle row) but with rescaled values.

≈ 5 min. In this study, we used the updated version of the vendor provided 3D-GRASE ASL sequence (Siemens Advanced 3D-ASL WIP), and no custom sequence developments were carried out to enable widespread usage without the necessity to developing custom MR sequences or image reconstruction, despite the continuous progress being made on the development of ASL methods (Hernandez-Garcia et al., 2022). Therefore, we expect the sequence parameter choices made in this study can be selected in the 3D-GRASE ASL sequence available from the vendor on most modern scanners. We show that the increased spatial resolution does result in a reduction of partial voluming compared to the default clinical protocol. We show that through-plane blurring is a problem for 3D-GRASE ASL independent of the protocol being used. We find z-deblurring to be more effective on the hires than the clinical data. Finally, the choice of head coil for imaging perfusion with ASL at 3 T does play an important role with 32 and 64 ch being particularly well suited. Consistent with the results of deblurring, the hires datasets benefit most from perfusion tSNR improvements with higher coil counts.

4.1 Impact of spatial resolution on ASL imaging

We show that increasing the spatial resolution of ASL 5.78×, the clinical resolution does not have a detrimental effect on the measuring perfusion (Figure 1) and takes the same duration as a clinical scan (≈ 5 min). The mean perfusion-weighting values in the high-resolution data were found to be similar to the clinical data (e.g., 32 channel: 608.55 ± 256.24 vs. 605.91 ± 313.30 a. u.) (Supplementary Table S4). Importantly, however, the hires perfusion-weighted images exhibited approximately 27% greater IQR (32ch: clinical 334.3 vs. 423.67 a. u.) than the clinical data. As the IQR is a measure of spread around the mean, this measure is indicative of the dynamic range of perfusion in the data. Being capable of resolving a wider range of perfusion values is critical to detect subtle abnormalities and early detection of neurological diseases (Clement et al., 2018), therefore emphasizing the importance of high spatial resolution imaging (Mora Álvarez et al., 2019) in clinical research and cognitive neuroscience applications.

Acquiring data at a higher spatial resolution supports the observed improvement in dynamic range and concurrently reduces PV effects. The cortical GM is bound on either side by WM and CSF, and PV occurs when a GM voxel contains fractional distributions from these adjacent tissue classes that influence cortical perfusion measures. Figure 2 shows that hires ASL data consistently yield a greater volume of "pure" tissue voxels than the clinical data (GM: ≈ 6713 mm^3, WM: ≈ 16,938 mm^3, CSF: ≈ 15,422 mm^3) (It is to be noted that these PV fractions were derived from a dilated, cortical GM ROI, that is, the ROI does not consist of the large ventricles or the majority of WM in the brain). The increased number of "pure" WM and CSF voxels indicates that the hires data can enable a more effective separation of non-GM signal contributors to the perfusion signal of interest.

Partial volume correction was not performed at any stage of processing of the datasets (Chappell et al., 2011; Chappell et al., 2021). In the absence of PV correction of the lower resolution clinical protocol data, the lower CBF in WM partial voluming with GM would result in a reduction of the average CBF in GM. However, PV of GM with CSF (or rather vessels in CSF) can have the opposite effect, resulting in higher than expected CBF values in GM, which is likely the case here. It is also important to note the default clinical protocol was not subject to any optimization in the present work. Although seemingly contrary to expectations, for

parameter sets similar to the default clinical protocol, the CBF values in our data are consistent with those of studies that use a similar sequence (Vidorreta et al., 2014). Other reasons could be the fact that high-resolution acquisitions inherently reduce partial voluming effects and, therefore, can be more sensitive to the CBF variability within GM. Maps including that of the perfusion weighting and rCBF are shown in Supplementary Figures S1 (clinical vs. hires) and Supplementary Figure S2 (pCASL vs. PASL). We found that the hires PASL results are in good agreement with the hires pCASL (Supplementary Figure S2). Consistent with the previous work (Wu et al., 2007; Chen et al., 2011), the pCASL labeling scheme exhibits approximately 22%–26% higher perfusion tSNR than FAIR-Q2TIPS for the hires acquisitions in our study.

4.2 Impact of deblurring on 3D-GRASE ASL data

Because high spatial resolution is required, the total echo-train length (TE × TF) can exceed 300 ms ($\gg \pi \times T_2^*$ of tissue), resulting in increased blurring (Qin, 2012; Liang et al., 2014; Zhao et al., 2018), that occurs maximally in the slice direction (through-plane or *z*-axis). Thus, requiring post-processing correction or making compromises would render whole-brain acquisitions infeasible. We find that the application of z-deblurring has a demonstrable effect on the improvement of the spatial fidelity (or reducing the estimated FWHM) of the ASL data, as shown in Table 2. It is interesting to note that FWHM along z for the deblurred clinical data (5.22 ± 0.49 mm) is still larger than the non-deblurred hires data (4.01 ± 0.31 mm). This has an important implication in clinical settings where advanced image post-processing is often unavailable. Importantly, the hires ASL protocols enable researchers and clinicians to resolve perfusion changes with a higher spatial fidelity (without requiring advanced image processing) than the *post hoc* deblurred clinical datasets. Furthermore, post-processing deblurring methods have their limitations and they cannot synthesize resolution from information lost in acquisition. Although lengthening the echo-train is an important concern, our findings (Table 2) indicate that deblurring methods are more effective for high-resolution ASL imaging.

4.3 Impact of coil choice on ASL imaging

We demonstrate that robust rCBF maps can be acquired independently of the coil choice (Figure 1); however, higher coil counts (32 and 64ch) offer substantial gains in perfusion tSNR than the 20ch coil (Figure 4). We find that increasing coil count results in ≈ 2–2.5% gain in perfusion tSNR for the clinical protocol compared to ≈ 34–42% gain for the hires protocol (Supplementary Table S5). One reason for this difference could be that data acquired with clinical protocol in Figure 1 are relatively insensitive to the choice of coil due to its low spatial resolution (i.e., low thermal noise) and acceleration (i.e., no g-factor penalty) requirements. On the other hand, the hires protocols accelerate higher and have increased thermal noise than the clinical protocol, owing to the smaller voxel sizes, and therefore benefit from the increased number of coils (Figure 4).

Interestingly, Figure 4 shows that reducing the voxel size (i.e., higher spatial resolution) actually results in a gain in perfusion SNR (clinical vs. hires (scaled)), which may seem counterintuitive from the standpoint of conventional fMRI where the SNR of the BOLD signal decreases with increasing resolution. However, this is due to the different signal origins of the BOLD and perfusion contrasts. By reducing PV with veins and macro-vasculature, we are reducing the signal contributors of the BOLD signal, whereas these same signal components are sources of noise in perfusion imaging, as they have very low perfusion signals. In addition, reducing WM contribution of voxels dominated by GM improves the fidelity of GM perfusion values and reduced influence of physical noise stemming from WM. Therefore, reducing PV increases our sensitivity to the cortical microvasculature signal and reduces noise and signal contribution from WM and CSF. In other words, higher spatial resolution not only decreases image SNR in both BOLD and perfusion methods due to reduction in the number of protons (i.e., voxel volume) but also reduces noise sources in perfusion imaging stemming from CSF, veins, and WM.

4.4 Limitations

Although we demonstrate clear benefits of high-resolution ASL imaging for clinical research and cognitive neuroscience applications (group studies), the present study is limited in its ability to comment on a potential impact in daily clinical practice (single subject, diagnostic). Nevertheless, we believe future studies investigating the impact of ASL sequence parameters in routine clinical practice should use a modestly higher isotropic resolution (e.g., 2.5 mm) to enable better visualization of localized differences in perfusion. Here, we also opted for modest acceleration schemes (Table 1) as the protocols were to be compared on all three available head coils and the 20ch coil would be the lowest common denominator. The availability of the 3D-GRASE readout with 2D-CAIPIRINHA undersampling enabled us to achieve higher isotropic spatial resolution for perfusion imaging (Vidorreta et al., 2014; Ivanov et al., 2017; Boland et al., 2018). For a future non-comparison type of study, this protocol optimization can be pushed further to take advantage of the higher coil count and achieve higher acceleration. A systematic exploration of different CAIPI acceleration schemes or trajectories, impact of reduced g-factor noise amplification on image quality, is, unfortunately, beyond the scope of the present work.

4.5 Concluding remarks

Taking together, this study demonstrates the feasibility and benefits of imaging perfusion using high-resolution isotropic ASL for clinical research and cognitive neuroscience applications at 3 T. We have shown that increasing the spatial resolution does not compromise the accuracy and quality of the perfusion maps, and allows for a wider dynamic range of perfusion values. We have shown that high-resolution data can more effectively separate out the non-GM signal contributors (reduce PV effects), which improves the sensitivity to cortical microvasculature and tissue in GM. In addition, post-processing methods such as z-deblurring are

important considerations for whole-brain perfusion imaging using 3D-GRASE ASL to improve the spatial fidelity of the data. High-resolution acquisitions take advantage of the higher coil counts and offer substantial gains in perfusion tSNR with 32 and 64ch coils. Echoing what Donahue and colleagues envisioned in 2006, we strongly believe that high-resolution ASL (2–2.5 mm isotropic) can be a new standard for perfusion imaging using ASL at 3 T and be adopted into clinical and cognitive neuroscience research workflows.

Data availability statement

Data from this study can be accessed via the Canadian Open Neuroscience Platform (https://n2t.net/ark:/70798/d7mfwmtmr15hw6xwwg).

Ethics statement

The studies involving humans were approved by the Research Ethics Board of University Health Network according to the guidelines of Health Canada. The studies were conducted in accordance with the local legislation and institutional requirements. The participants provided their written informed consent to participate in this study.

Author contributions

SK: conceptualization, data curation, formal analysis, investigation, methodology, visualization, writing–original draft, and writing–review and editing. ÍO: investigation, methodology, validation, visualization, writing–original draft, and writing–review and editing. KU: conceptualization, funding acquisition, methodology, project administration, resources, supervision, writing–original draft, and writing–review and editing.

Funding

The author(s) declare financial support was received for the research, authorship, and/or publication of this article. The study was supported by the Institute for Basic Science, Suwon, Republic of Korea (IBS-R015-D1) to KU.

Acknowledgments

The authors thank Asma Naheed, MRT for the scanning support at the Slaight Family Centre for Advanced MRI, Toronto Western Hospital, University Health Network, Toronto, Canada. They would like to thank Dr. Thomas F. Kirk for the invaluable discussions about the partial voluming problem in ASL MRI data. They would like to thank Dr. Dimo Ivanov for his insights into ASL acquisition. They thank Dr. Gerald R. Moran and Dr. Josef Pfeuffer for their collaboration and for providing the Advanced 3D ASL WIP package for the Siemens XA30 platform.

Conflict of interest

The authors declare that the research was conducted in the absence of any commercial or financial relationships that could be construed as a potential conflict of interest.

Publisher's note

Supplementary material

The Supplementary Material for this article can be found online at: https://www.frontiersin.org/articles/10.3389/fphys.2023.1271254/full#supplementary-material

References

Alsop, D. C., Detre, J. A., Golay, X., Günther, M., Hendrikse, J., Hernandez-Garcia, L., et al. (2015). Recommended implementation of arterial spin-labeled perfusion MRI for clinical applications: a consensus of the ISMRM perfusion study group and the european consortium for ASL in dementia. *Magn. Reson. Med.* 73, 102–116. doi:10.1002/mrm.25197

Andersson, J. L., Skare, S., and Ashburner, J. (2003). How to correct susceptibility distortions in spin-echo echo-planar images: application to diffusion tensor imaging. *Neuroimage* 20, 870–888. doi:10.1016/S1053-8119(03)00336-7

Asllani, I., Borogovac, A., and Brown, T. R. (2008). Regression algorithm correcting for partial volume effects in arterial spin labeling mri. *Magnetic Reson. Med.* 60, 1362–1371. doi:10.1002/mrm.21670

Avants, B. B., Tustison, N. J., Song, G., Cook, P. A., Klein, A., and Gee, J. C. (2011). A reproducible evaluation of ants similarity metric performance in brain image registration. *Neuroimage* 54, 2033–2044. doi:10.1016/j.neuroimage.2010.09.025

Avants, B. B., Tustison, N. J., Stauffer, M., Song, G., Wu, B., and Gee, J. C. (2014). The Insight ToolKit image registration framework. *Front. Neuroinform.* 8, 44. doi:10.3389/fninf.2014.00044

Boland, M., Stirnberg, R., Pracht, E. D., Kramme, J., Viviani, R., Stingl, J., et al. (2018). Accelerated 3d-grase imaging improves quantitative multiple post labeling delay arterial spin labeling. *Magnetic Reson. Med.* 80, 2475–2484. doi:10.1002/mrm.27226

Buxton, R. B., Frank, L. R., Wong, E. C., Siewert, B., Warach, S., and Edelman, R. R. (1998). A general kinetic model for quantitative perfusion imaging with arterial spin labeling. *Magn. Reson Med.* 40, 383–396. doi:10.1002/mrm.1910400308

Chappell, M. A., Groves, A. R., MacIntosh, B. J., Donahue, M. J., Jezzard, P., and Woolrich, M. W. (2011). Partial volume correction of multiple inversion time arterial spin labeling mri data. *Magn. Reson Med.* 65, 1173–1183. doi:10.1002/mrm.22641

Chappell, M. A., Groves, A. R., Whitcher, B., and Woolrich, M. W. (2009). Variational bayesian inference for a nonlinear forward model. *Trans. Sig. Proc.* 57, 223–236. doi:10.1109/TSP.2008.2005752

Chappell, M. A., Kirk, T. F., Craig, M. S., McConnell, F. A. K., Zhao, M. Y., MacIntosh, B. J., et al. (2023). BASIL: A toolbox for perfusion quantification using arterial spin labelling. *Imaging Neurosci.* 1, 1–16. doi:10.1162/imag_a_00041

Chappell, M. A., McConnell, F. A., Golay, X., Günther, M., Hernandez-Tamames, J. A., van Osch, M. J., et al. (2021). Partial volume correction in arterial spin labeling perfusion mri: a method to disentangle anatomy from physiology or an analysis step too far? *Neuroimage* 238, 118236. doi:10.1016/j.neuroimage.2021.118236

Chen, Y., Wang, D. J., and Detre, J. A. (2011). Test-retest reliability of arterial spin labeling with common labeling strategies. *J. Magnetic Reson. Imaging* 33, 940–949. doi:10.1002/jmri.22345

Clement, P., Castellaro, M., Okell, T., Thomas, D. L., Vandemaele, P., Elgayar, S., et al. (2022). Asl-bids, the brain imaging data structure extension for arterial spin labeling. *Sci. Data* 9, 543. doi:10.1038/s41597-022-01615-9

Clement, P., Mutsaerts, H. J., Václavů, L., Ghariq, E., Pizzini, F. B., Smits, M., et al. (2018). Variability of physiological brain perfusion in healthy subjects - a systematic review of modifiers. considerations for multi-center asl studies. *J. Cereb. Blood Flow Metabolism* 38, 1418–1437. doi:10.1177/0271678X17702156

Cox, R. W. (1996). AFNI: software for analysis and visualization of functional magnetic resonance neuroimages. *Comput. Biomed. Res.* 29, 162–173. doi:10.1006/cbmr.1996.0014

Cox, R. W., Chen, G., Glen, D. R., Reynolds, R. C., and Taylor, P. A. (2017). FMRI clustering in AFNI: false-positive rates redux. *Brain Connect.* 7, 152–171. doi:10.1089/brain.2016.0475

Cox, R. W., and Hyde, J. S. (1997). Software tools for analysis and visualization of fmri data. *NMR Biomed.* 10, 171–178. doi:10.1002/(sici)1099-1492(199706/08)10:4/5<171::aid-nbm453>3.0.co;2-l

Dale, A. M., Fischl, B., and Sereno, M. I. (1999). Cortical surface-based analysis. i. segmentation and surface reconstruction. *Neuroimage* 9, 179–194. doi:10.1006/nimg.1998.0395

Detre, J. A., Leigh, J. S., Williams, D. S., and Koretsky, A. P. (1992). Perfusion imaging. *Magn. Reson Med.* 23, 37–45. doi:10.1002/mrm.1910230106

Detre, J. A., Rao, H., Wang, D. J. J., Chen, Y. F., and Wang, Z. (2012). Applications of arterial spin labeled mri in the brain. *J. Magn. Reson Imaging* 35, 1026–1037. doi:10.1002/jmri.23581

Donahue, M. J., Lu, H., Jones, C. K., Pekar, J. J., and van Zijl, P. C. (2006). An account of the discrepancy between mri and pet cerebral blood flow measures. a high-field mri investigation. *NMR Biomed.* 19, 1043–1054. doi:10.1002/nbm.1075

Feinberg, D. A., Ramanna, S., and Guenther, M. (2009). "Evaluation of new asl 3d grase sequences using parallel imaging, segmented and interleaved k-space at 3T with 12- and 32-channel coils," in Proceedings of the 17Th Annual Meeting of ISMRM, Honolulu, Hawaii, USA. (Honolulu, Hawaii, USA).

Fernández-Seara, M. A., Edlow, B. L., Hoang, A., Wang, J., Feinberg, D. A., and Detre, J. A. (2008). Minimizing acquisition time of arterial spin labeling at 3T. *Magn. Reson Med.* 59, 1467–1471. doi:10.1002/mrm.21633

Fischl, B., Salat, D. H., Busa, E., Albert, M., Dieterich, M., Haselgrove, C., et al. (2002). Whole brain segmentation: automated labeling of neuroanatomical structures in the human brain. *Neuron* 33, 341–355. doi:10.1016/s0896-6273(02)00569-x

Fischl, B., Sereno, M. I., and Dale, A. M. (1999). Cortical surface-based analysis. ii: inflation, flattening, and a surface-based coordinate system. *Neuroimage* 9, 195–207. doi:10.1006/nimg.1998.0396

Fonov, V., Evans, A., McKinstry, R., Almli, C., and Collins, D. (2009). Unbiased nonlinear average age-appropriate brain templates from birth to adulthood. *NeuroImage* 47, S102. doi:10.1016/S1053-8119(09)70884-5

Fonov, V., Evans, A. C., Botteron, K., Almli, C. R., McKinstry, R. C., Collins, D. L., et al. (2011). Unbiased average age-appropriate atlases for pediatric studies. *Neuroimage* 54, 313–327. doi:10.1016/j.neuroimage.2010.07.033

Greve, D. N., and Fischl, B. (2009). Accurate and robust brain image alignment using boundary-based registration. *Neuroimage* 48, 63–72. doi:10.1016/j.neuroimage.2009.06.060

Groves, A. R., Chappell, M. A., and Woolrich, M. W. (2009). Combined spatial and non-spatial prior for inference on mri time-series. *Neuroimage* 45, 795–809. doi:10.1016/j.neuroimage.2008.12.027

Hernandez-Garcia, L., Aramendia-Vidaurreta, V., Bolar, D. S., Dai, W., Fernández-Seara, M. A., Guo, J., et al. (2022). Recent technical developments in ASL: a review of the state of the art. *Magnetic Reson. Med.* 88, 2021–2042. doi:10.1002/mrm.29381

Hoopes, A., Mora, J. S., Dalca, A. V., Fischl, B., and Hoffmann, M. (2022). Synthstrip: skull-stripping for any brain image. *NeuroImage* 260, 119474. doi:10.1016/j.neuroimage.2022.119474

Iutaka, T., de Freitas, M. B., Omar, S. S., Scortegagna, F. A., Nael, K., Nunes, R. H., et al. (2023). Arterial spin labeling: techniques, clinical applications, and interpretation. *RadioGraphics* 43, e220088. doi:10.1148/rg.220088

Ivanov, D., Kashyap, S., Haast, R. A., Janssens, S., Huber, L., Poser, B. A., et al. (2018). "Whole-brain sub-millimeter isotropic resolution cerebral blood flow map in humans," in Proceedings of the Annual Meeting of the International Society for Magnetic Resonance in Medicine (ISMRM), Paris, France, 2301.

Ivanov, D., Pfeuffer, J., Gardumi, A., Uludağ, K., and Poser, B. A. a. (2017). "2d caipirinha improves accelerated 3d grase asl," in Proceedings of the Annual Meeting of the International Society for Magnetic Resonance in Medicine (ISMRM), Honolulu, USA, 3630.

Kashyap, S., Ivanov, D., Haast, R. A. M., Fritz, F. J., Harms, R. L., Huber, L., et al. (2022). "The impact of optimal RF coil combination on whole-brain sub-millimetre resolution perfusion imaging at 7T," in Proceedings of the Annual Meeting of the International Society for Magnetic Resonance in Medicine (ISMRM), London, UK, 1145.

Kashyap, S., Ivanov, D., Havlicek, M., Huber, L., Poser, B. A., and Uludağ, K. (2021). Sub-millimetre resolution laminar fMRI using arterial spin labelling in humans at 7 T. *PLOS ONE* 16, e0250504. doi:10.1371/journal.pone.0250504

Kim, S.-G. (1995). Quantification of relative cerebral blood flow change by flow-sensitive alternating inversion recovery (FAIR) technique: application to functional mapping. *Magnetic Reson. Med.* 34, 293–301. doi:10.1002/mrm.1910340303

Kirk, T., McConnell, F. K., Ivanov, D., Kashyap, S., Craig, M., and Chappell, M. (2020a). "Partial volume effect correction of arterial spin labelling data using surface segmentations," in Proceedings of the Annual Meeting of the International Society for Magnetic Resonance in Medicine (ISMRM) (Virtual), 3292.

Kirk, T. F., Coalson, T. S., Craig, M. S., and Chappell, M. A. (2020b). Toblerone: surface-based partial volume estimation. *IEEE Trans. Med. Imaging* 39, 1501–1510. doi:10.1109/TMI.2019.2951080

Liang, X., Connelly, A., Tournier, J.-D., and Calamante, F. (2014). A variable flip angle-based method for reducing blurring in 3d grase asl. *Phys. Med. Biol.* 59, 5559–5573. doi:10.1088/0031-9155/59/18/5559

Lindner, T., Bolar, D. S., Achten, E., Barkhof, F., Bastos-Leite, A. J., Detre, J. A., et al. (2023). Current state and guidance on arterial spin labeling perfusion mri in clinical neuroimaging. *Magnetic Reson. Med.* 89, 2024–2047. doi:10.1002/mrm.29572

Luh, W.-M., Wong, E. C., Bandettini, P. A., and Hyde, J. S. (1999). QUIPSS II with thin-slice TI1 periodic saturation: a method for improving accuracy of quantitative perfusion imaging using pulsed arterial spin labeling. *Magnetic Reson. Med.* 41, 1246–1254. doi:10.1002/(sici)1522-2594(199906)41:6<1246::aid-mrm22>3.0.co;2-n

Marques, J. P., Kober, T., Krueger, G., van der Zwaag, W., Van de Moortele, P.-F., and Gruetter, R. (2010). Mp2rage, a self bias-field corrected sequence for improved segmentation and t1-mapping at high field. *Neuroimage* 49, 1271–1281. doi:10.1016/j.neuroimage.2009.10.002

Mora Álvarez, M. G., Stobbe, R. W., and Beaulieu, C. (2019). High resolution continuous arterial spin labeling of human cerebral perfusion using a separate neck tagging RF coil. *PLoS ONE* 14, e0215998. doi:10.1371/journal.pone.0215998

Paschoal, A. M., Leoni, R. F., Pastorello, B. F., and van Osch, M. J. P. (2021). Three-dimensional gradient and spin-echo readout for time-encoded pseudo-continuous arterial spin labeling: influence of segmentation factor and flow compensation. *Magnetic Reson. Med.* 86, 1454–1462. doi:10.1002/mrm.28807

Poser, B. A., Koopmans, P. J., Witzel, T., Wald, L. L., and Barth, M. (2010). Three-dimensional echo-planar imaging at 7 tesla. *NeuroImage* 51, 261–266. doi:10.1016/j.neuroimage.2010.01.108

Qin, Q. (2012). Point spread functions of the t2 decay in k-space trajectories with long echo train. *Magn. Reson. Imaging* 30, 1134–1142. doi:10.1016/j.mri.2012.04.017

Smith, S. M., Jenkinson, M., Woolrich, M. W., Beckmann, C. F., Behrens, T. E., Johansen-Berg, H., et al. (2004). Advances in functional and structural mr image analysis and implementation as fsl. *Neuroimage* 23, S208–S219. doi:10.1016/j.neuroimage.2004.07.051

Tan, H., Hoge, W., Hamilton, C., Günther, M., and Kraft, R. (2011). 3d grase propeller: improved image acquisition technique for arterial spin labeling perfusion imaging. *Magnetic Reson. Med.* 66, 168–173. doi:10.1002/mrm.22768

Tisdall, M. D., Hess, A. T., Reuter, M., Meintjes, E. M., Fischl, B., and van der Kouwe, A. J. (2012). Volumetric navigators for prospective motion correction and selective reacquisition in neuroanatomical mri. *Magn. Reson Med.* 68, 389–399. doi:10.1002/mrm.23228

Tisdall, M. D., Reuter, M., Qureshi, A., Buckner, R. L., Fischl, B., and van der Kouwe, A. J. W. (2016). Prospective motion correction with volumetric navigators (vnavs) reduces the bias and variance in brain morphometry induced by subject motion. *Neuroimage* 127, 11–22. doi:10.1016/j.neuroimage.2015.11.054

van der Kouwe, A. J. W., Benner, T., Salat, D. H., and Fischl, B. (2008). Brain morphometry with multiecho mprage. *Neuroimage* 40, 559–569. doi:10.1016/j.neuroimage.2007.12.025

Vidorreta, M., Balteau, E., Wang, Z., De Vita, E., Pastor, M. A., Thomas, D. L., et al. (2014). Evaluation of segmented 3d acquisition schemes for whole-brain high-resolution arterial spin labeling at 3 t. *NMR Biomed.* 27, 1387–1396. doi:10.1002/nbm.3201

Williams, D. S., Detre, J. A., Leigh, J. S., and Koretsky, A. P. (1992). Magnetic resonance imaging of perfusion using spin inversion of arterial water. *Proc. Natl. Acad. Sci. U. S. A.* 89, 212–216. doi:10.1073/pnas.89.1.212

Wong, E. C., Buxton, R. B., and Frank, L. R. (1997). Implementation of quantitative perfusion imaging techniques for functional brain mapping using pulsed arterial spin labeling. *NMR Biomed.* 10, 237–249. doi:10.1002/(sici)1099-1492(199706/08)10:4/5⟨237::aid-nbm475⟩3.0.co;2-x

Wong, E. C., Buxton, R. B., and Frank, L. R. (1998). Quantitative imaging of perfusion using a single subtraction (QUIPSS and QUIPSS II). *Magnetic Reson. Med.* 39, 702–708. doi:10.1002/mrm.1910390506

Wu, W.-C., Fernandez-Seara, M., Detre, J. A., Wehrli, F. W., and Wang, J. (2007). A theoretical and experimental investigation of the tagging efficiency of pseudocontinuous arterial spin labeling. *Magnetic Reson. Med.* 58, 1020–1027. doi:10.1002/mrm.21403

Zhang, Y., Brady, M., and Smith, S. (2001). Segmentation of brain mr images through a hidden markov random field model and the expectation-maximization algorithm. *IEEE Trans. Med. Imaging* 20, 45–57. doi:10.1109/42.906424

Zhao, L., Chang, C.-Y. E., and Alsop, D. C. (2018). Controlling t2 blurring in 3d rare arterial spin labeling acquisition through optimal combination of variable flip angles and k-space filtering. *Magnetic Reson. Med.* 80, 1391–1401. doi:10.1002/mrm.27118

Zuo, Z., Wang, R., Zhuo, Y., Xue, R., Lawrence, K. S. S., and Wang, D. J. J. (2013). Turbo-FLASH based arterial spin labeled perfusion MRI at 7 t. *PLOS ONE* 8, e66612. doi:10.1371/journal.pone.0066612